**Astronomy
&
Astrophysics**

The *Herschel* Virgo Cluster Survey[⋆],[⋆⋆]

XV. *Planck* submillimetre sources in the Virgo Cluster

M. Baes[1], D. Herranz[2], S. Bianchi[3], L. Ciesla[4], M. Clemens[5], G. De Zotti[5], F. Allaert[1], R. Auld[6], G. J. Bendo[7],
M. Boquien[8], A. Boselli[8], D. L. Clements[9], L. Cortese[10], J. I. Davies[6], I. De Looze[1], S. di Serego Alighieri[3], J. Fritz[1],
G. Gentile[1,11], J. González-Nuevo[2], T. Hughes[1], M. W. L. Smith[6], J. Verstappen[1], S. Viaene[1], and C. Vlahakis[12]

[1] Sterrenkundig Observatorium, Universiteit Gent, Krijgslaan 281, 9000 Gent, Belgium
    e-mail: maarten.baes@ugent.be
[2] Instituto de Física de Cantabria (CSIC-UC), Avda. los Castros s/n, 39005 Santander, Spain
[3] INAF – Osservatorio Astrofisico di Arcetri, Largo E. Fermi 5, 50125 Florence, Italy
[4] University of Crete, Department of Physics, 71003 Heraklion, Greece
[5] INAF – Osservatorio Astronomico di Padova, vicolo dell'Osservatorio 5, 35122 Padova, Italy
[6] School of Physics and Astronomy, Cardiff University, Queens Buildings, The Parade, Cardiff CF24 3AA, UK
[7] UK ALMA Regional Centre Node, Jodrell Bank Centre for Astrophysics, School of Physics and Astronomy,
    University of Manchester, Oxford Road, Manchester M13 9PL, UK
[8] Aix-Marseille Université, CNRS, LAM (Laboratoire d'Astrophysique de Marseille) UMR 7326, 13388 Marseille, France
[9] Imperial College London, Blackett Laboratory, Prince Consort Road, London SW7 2AZ, UK
[10] Centre for Astrophysics and Supercomputing, Swinburne University of Technology, Hawthorn VIC 3122, Australia
[11] Department of Physics and Astrophysics, Vrije Universiteit Brussel, Pleinlaan 2, 1050 Brussel, Belgium
[12] Joint ALMA Observatory/European Southern Observatory, 3107 Alonso de Córdova, Vitacura, Santiago, Chile

ABSTRACT

We cross-correlate the *Planck* Catalogue of Compact Sources (PCCS) with the fully sampled 84 deg^2 *Herschel* Virgo Cluster Survey (HeViCS) fields. We search for and identify the 857 and 545 GHz PCCS sources in the HeViCS fields by studying their FIR/submm and optical counterparts. We find 84 and 48 compact *Planck* sources in the HeViCS fields at 857 and 545 GHz, respectively. Almost all sources correspond to individual bright Virgo Cluster galaxies. The vast majority of the *Planck* detected galaxies are late-type spirals, with the Sc class dominating the numbers, while early-type galaxies are virtually absent from the sample, especially at 545 GHz. We compare the HeViCS SPIRE flux densities for the detected galaxies with the four different PCCS flux density estimators and find an excellent correlation with the aperture photometry flux densities, even at the highest flux density levels. We find only seven PCCS sources in the HeViCS fields without a nearby galaxy as obvious counterpart, and conclude that all of these are dominated by Galactic cirrus features or are spurious detections. No *Planck* sources in the HeViCS fields seem to be associated to high-redshift proto-clusters of dusty galaxies or strongly lensed submm sources. Finally, our study is the first empirical confirmation of the simulation-based estimated completeness of the PCCS, and provides a strong support of the internal PCCS validation procedure.

Key words. galaxies: ISM – submillimeter: galaxies

1. Introduction

Roughly half of all the energy emitted by stars and AGNs in the Universe has been absorbed by dust and re-emitted at far-infrared (FIR) and submillimetre (submm) wavelengths. For many years, this important wavelength regime was one of the least explored windows. Several space missions have been operational in the FIR wavelength region since the mid 1980s, including the Infrared Astronomical Satellite (IRAS, Neugebauer et al. 1984), the Infrared Space Observatory (ISO, Kessler et al. 1996), the *Spitzer* Space Telescope (Werner et al. 2004) and the Akari mission (Murakami et al. 2007). At the same time, the submm window has been explored using bolometer instruments

on ground-based telescopes including SCUBA and SCUBA-2 on the *James Clerck Maxwell* Telescope (Holland et al. 1999, 2006) and LABOCA on the Atacama Pathfinder Experiment (Siringo et al. 2009), as well as balloon experiments such as the Balloon-borne Large Aperture Submillimeter Telescope (BLAST, Pascale et al. 2008). All these missions suffered from relatively poor resolution and/or sensitivity, and left the wavelength region between 200 and 800 μm virtually unexplored. The simultaneous launch of the *Herschel* Space Observatory (Pilbratt et al. 2010) and the *Planck* mission (Planck Collaboration 2011a) in May 2009 has finally opened the FIR/submm window in earnest.

Herschel was a FIR/submm observatory facility that has offered for the first time imaging and spectroscopic capabilities from space in the wavelength range between 55 and 671 μm. It contained three instruments on board: the FIR imager and spectrometer PACS (Poglitsch et al. 2010), the submm imager and spectrometer SPIRE (Griffin et al. 2010), and the high-resolution

---

heterodyne spectrometer HIFI (de Graauw et al. 2010). The PACS camera had three photometric bands, centered at 70, 100 and 160 μm, the corresponding SPIRE camera operates at three bands centered at 250, 350 and 500 μm. The angular resolution of the *Herschel* imaging data varies from 6 arcsec at the PACS 70 μm band to 36 arcsec at the SPIRE 500 μm band. The main goal of *Herschel* was to study the cool interstellar dust and gas in the Universe, with pointed observations of all types of objects, ranging from the Solar System (e.g., Müller et al. 2010; Hartogh et al. 2011) to the deep extragalactic sky (e.g., Maddox et al. 2010; Oliver et al. 2012; Thacker et al. 2013).

Planck is an all sky survey mission that has been simultaneously and continuously scanning the entire sky in nine submm/mm wavebands. It has two instruments onboard: the High Frequency Instrument (HFI, Lamarre et al. 2010) contains bolometers operational at six bands centered at 857, 545, 353, 217, 143 and 100 GHz (corresponding to wavelengths of 350, 550, 850 μm and 1.38, 2.1 and 3 mm, respectively) and the Low Frequency Instrument (LFI, Bersanelli et al. 2010) contains radiometers that cover three bands at 70, 44 and 30 GHz (corresponding to 4.3, 6.8 and 10 mm, respectively). The angular resolution decreases from 4.33 arcmin at the highest frequency to 32.88 arcmin at the lowest frequency. The prime objective of *Planck* is to measure the spatial anisotropies of the temperature and the polarization of the cosmic microwave background with an unprecedented sensitivity and resolution (Planck Collaboration XV, XVI. 2014). In addition, the *Planck* mission has produced a treasure of valuable information on the submm/mm properties of foreground objects, both in our Milky Way (e.g., Planck Collaboration 2011c,g,h) and extragalactic objects (e.g., Planck Collaboration 2011d,e; Clemens et al. 2013). A preliminary catalogue of *Planck* compact sources, the Early Release Compact Source Catalogue (ERCSC) was publicly released in January 2011 and contains more than 15 000 unique sources (Planck Collaboration 2011b). A similar, but more complete catalogue (more than 25 000 sources), the *Planck* Catalogue of Compact Sources (PCCS, Planck Collaboration XXVIII. 2014), was released in March 2013 as part of the major *Planck* 2013 data and scientific results release (Planck Collaboration I. 2014).

The complementarity and overlap of the *Planck* and *Herschel* missions offers a number of advantages. *Planck* has the advantage of observing the entire sky, and is likely to discover the most rare and extreme submm sources, including strongly lensed high-redshift starburst galaxies and proto-clusters of luminous submm galaxies. With its much better spatial resolution, *Herschel* has been ideal to follow up these sources, to determine their nature and to characterize their physical properties (the ERCSC was released a few months before *Herschel*'s second inflight announcement of opportunity for observing time proposals). More generally, *Herschel* observations of *Planck* sources are useful to quantify the boosting of *Planck* flux densities due to noise peaks and confusion, to provide more accurate positions, and to distinguish between Galactic foreground cirrus and genuine extragalactic point sources. *Herschel* can also take advantage of the absolute calibration of the *Planck* HFI instrument. Finally, while both missions have a limited overlap in wavelength coverage, they can take advantage of the complementarity beyond this common range. For *Herschel* sources, *Planck* flux densities at frequencies of 545 GHz and lower (i.e. wavelengths of 550 μm and beyond) can be useful to investigate a change in the slope of the spectral energy distribution (SED) of galaxies at about 500 μm that might be related to very cold dust or might originate from dust with a shallow emissivity function. In turn,

SPIRE 250 μm and PACS data are useful to bridge the gap in the SED between the *Planck* HFI and the 100 μm band as observed by IRAS.

The complementarity of *Herschel* and *Planck* can be exploited in different ways. A first obvious way is to consider a set of galaxies observed by *Herschel* and complement the *Herschel* data with *Planck* observations. This approach has been applied to several samples of nearby galaxies (e.g., Ciesla et al. 2012; Davies et al. 2012; Planck Collaboration XVI. 2014), either as a check on the *Herschel* photometry or to add additional submm data to the SED beyond the SPIRE 500 μm limit. The disadvantage of this approach is that the population of galaxies is fixed beforehand (typically selected in the optical), and hence does not allow for a characterization of the *Planck* population or a discovery of peculiar *Planck* sources. An alternative approach is to search for and characterize the *Planck* sources in large-area "blind" extragalactic surveys with *Herschel*. A first effort along this line is the recent work by Herranz et al. (2013). They cross-correlate the *Planck* ERCSC catalogue with *Herschel* observations taken as part of the *Herschel* Astrophysical Terahertz Large Area Survey (H-ATLAS, Eales et al. 2010). H-ATLAS is a *Herschel* open time key programme that has surveyed about 550 deg^2 of extragalactic sky in five FIR/submm bands, using the PACS and SPIRE instruments in parallel mode. Herranz et al. (2013) analyzed the compact *Planck* submm sources in the so-called Phase 1 fields, a set of equatorial fields with a total survey area of 134.5 deg^2. They detected 28 compact *Planck* sources, 16 of which are most probably high-latitude Galactic cirrus features. Ten of the *Planck* sources correspond to bright, low-redshift galaxies and one source corresponds to a pair of nearby galaxies. Interestingly, one compact *Planck* source is resolved by *Herschel* into a condensation of about 15 faint point sources surrounding an unusually bright submm source, which turned out to be a strongly lensed submm galaxy at $z = 3.259$ (Fu et al. 2012; Harris et al. 2012).

In this paper, we investigate the *Planck* compact submm sources in the survey field of another *Herschel* extragalactic survey, the *Herschel* Virgo Cluster Survey (HeViCS, Davies et al. 2010). HeViCS is a *Herschel* open time key program and has conducted a deep survey of four 16 deg^2 fields in the Virgo Cluster. The prime aim of HeViCS is a detailed study of the FIR/submm properties of the galaxies in the Virgo Cluster (Cortese et al. 2010b; Smith et al. 2010; Grossi et al. 2010; Baes et al. 2010; De Looze et al. 2010; Magrini et al. 2011; Corbelli et al. 2012; Davies et al. 2012; di Serego Alighieri et al. 2013) and a study of the environmental effects through comparison with nearby galaxies in less dense environments, such as in the HRS (Boselli et al. 2010b, 2012; Ciesla et al. 2012) or KINGFISH (Kennicutt et al. 2011; Dale et al. 2012) surveys. However, given that HeViCS has observed a large area of extragalactic sky, it is very suitable for a cross-correlation between *Herschel* and *Planck*. Similar to H-ATLAS, HeViCS is a fully-sampled, blind survey and adopts parallel mode observations with both PACS and SPIRE at five wavelengths between 100 and 500 μm. The main difference between both surveys, apart from the choice of the survey fields and the specific scientific objectives, is the depth of the observations: while H-ATLAS uses two cross-linked scans of every field, HeViCS has performed eight cross-linked scans of every field, with the aim to reach the 250 μm confusion limit. Due to the time span between the different observations and the corresponding orientation of the survey fields and the spatial offset between the PACS and SPIRE instruments on the sky, HeViCS has observed a total area of 84 deg^2, of which 55 deg^2 has been observed to the full

depth (for details, see Auld et al. 2013). Combined with the fact that the Virgo Cluster has been observed extensively at virtually all wavelengths from X-rays to radio waves (e.g., Böhringer et al. 1994; Davies et al. 2004; Lawrence et al. 2007; Boselli et al. 2011; Ferrarese et al. 2012), the HeViCS fields are ideal for a flux density comparison between *Planck* and *Herschel* and a characterisation of the nature of the detected *Planck* submm sources within the survey field.

The content of this paper is as follows: in Sect. 2 we search for and characterize the PCCS 857 and 545 GHz sources in the HeViCS survey fields and we search for their *Herschel* FIR/submm and optical counterparts. In Sect. 3, we analyze different characteristics of these populations: we compare the various flavors of the flux densities from the PCCS of the *Planck* detected sources in the HeViCS fields to the corresponding SPIRE flux densities at 350 and 500 μm, discuss the nature of sources without obvious counterparts, we investigate the completeness and positional accuracy of the PCCS, and we discuss the overdensity of the Virgo Cluster at submm wavelengths. Finally, in Sect. 4 we present our conclusions and summary.

2. Identification and characterization of the sources

We searched the *Planck* Catalogue of Compact Sources (PCCS) for all sources within the boundaries of the 84 deg^2 extended HeViCS fields. In this section we identify these sources and discuss the global properties of the sample of detected 857 and 545 GHz sources.

2.1. 857 GHz sources

The dominant emission mechanism at 857 GHz (350 μm) is thermal dust emission. For realistic dust temperatures, 857 GHz is already significantly down the Rayleigh-Jeans tail of the blackbody spectrum, so we primarily expect emission by large amounts of cold dust, rather than warm dust emission linked to star formation (e.g., Bendo et al. 2010, 2012; Boquien et al. 2011). This frequency is still too high for free-free emission or synchrotron emission to start playing a significant role. On the other hand, thanks to the negative *K*-correction, galaxies at intermediate or high redshift can have the peak of their SED around 857 GHz or even lower frequencies, and star-forming galaxies at $z > 0.5$ form a substantial contribution to the galaxy population at the frequency of 857 GHz (e.g., Clements et al. 2010; Lapi et al. 2011). Strongly lensed ultra-luminous infrared galaxies at redshifts $z > 1$ could also contribute to the population (Negrello et al. 2007; Lapi et al. 2012). So we expect that the counterparts of the *Planck* sources at 857 GHz would be dominated by nearby galaxies, with a potential contribution of intermediate to high redshift galaxies (in particular if they tend to cluster within the relatively large *Planck* beam).

We used the online *Planck* Legacy Archive (PLA) tool to select from the PCCS 857 GHz catalogue those sources located in the extended HeViCS survey field. The search resulted in 84 compact *Planck* sources. In Table 1 we list each of these sources, with the central positions and flux densities as listed in the PCCS. Subsequently, we searched for optical and FIR/submm counterparts for each of these sources, using a simple query in the NASA/IPAC Extragalactic Database (NED) for sources within the 857 GHz beam FWHM and a search in the HeViCS *Herschel* maps. For 82 of the 84 sources detected at 857 GHz, we could immediately match the *Planck* source to

an optical and *Herschel* counterpart. Examples of such identifications of *Planck* sources are shown in Fig. 1.

In 80 cases the counterpart was a single nearby galaxy (top two rows of Fig. 1), and 77 of these belong to the Virgo Cluster. The three remaining ones are the background galaxies IC 3029, NGC 4246 and NGC 4334, at distances of about 98, 56 and 66 Mpc respectively (Springob et al. 2005, 2009; Mould et al. 2000).

The majority of these 80 nearby galaxies are late-type spiral galaxies, with the Sc class accounting for slightly more than 40% of all the *Planck* detected galaxies. Only three galaxies (NGC 4370, 4429 and 4526) are classified as lenticular in the Galaxy On Line Database Milano Network (GOLDMine, Gavazzi et al. 2003), and the first of these three is sometimes classified as Sa (e.g., de Vaucouleurs et al. 1991). The only elliptical galaxy detected at 857 GHz is M 87, the massive radio galaxy at the centre of the Virgo Cluster. Whether or not this galaxy has a substantial interstellar dust reservoir detectable at FIR/submm wavelengths is still a matter of debate, even with the *Herschel* data at hand (Baes et al. 2010; Boselli et al. 2010a; di Serego Alighieri et al. 2013). It is clear, however, that the emission at frequencies of 857 GHz and lower is dominated by synchrotron emission that goes as $S_\nu \propto \nu^\alpha$ with a spectral index $\alpha \approx -0.75$ (Shi et al. 2007; Buson et al. 2009; Cotton et al. 2009; Baes et al. 2010).

Two 857 GHz PCCS sources, PCCS1 857 G272.51+75.68 and G289.78+73.72, correspond to a galaxy pair rather than a single bright galaxy (bottom two rows of Fig. 1). The former corresponds to the close pair KPG 332, formed by the edge-on galaxy NGC 4302 and the inclined spiral NGC 4298, with a projected separation of 2.4 arcmin (recall that the *Planck*'s beam size at 857 GHz is 4.33 arcmin). The position of the *Planck* source is centered between the two galaxies, closer to NGC 4302, which is the most luminous of both sources at 350 μm (Davies et al. 2012; Auld et al. 2013). The latter *Planck* source PCCS1 857 G289.78+73.72 corresponds to the close pair VV 219, also known as the Siamese Twins. It consists of the two spiral galaxies NGC 4567 and 4568, with a separation of 1.3 arcmin. Here the position of the *Planck* source is close to the centre of NGC 4568, which is significantly more luminous than its companion at 350 μm (Davies et al. 2012; Auld et al. 2013).

The remaining two *Planck* detections at 857 GHz, PCCS1 857 G261.44+74.24 and G270.81+76.99, do not have any nearby galaxy as optical counterpart. Their nature will be discussed in Sect. 3.3.

2.2. 545 GHz sources

The dominant emission mechanism at 545 GHz (550 μm) is still thermal emission by cool, large dust. Due to the steep spectral slope of a modified blackbody at submm wavelengths, $F_\nu \propto \nu^{2+\beta}$ with $\beta \sim 1.5-2$ the emissivity index (Boselli et al. 2012; Smith et al. 2013), the fluxes of nearby dusty galaxies at 545 GHz are typically a factor 6 lower compared to 857 GHz, and we therefore expect a correspondingly lower number of HFI detections corresponding to local dusty galaxies. On the other hand, the negative *K*-correction is stronger at 545 GHz and the relative contribution of intermediate and high redshift galaxies to the population counts is expected to be larger.

Querying the *Planck* PCCS catalogue through the PLA tool, we found 48 compact *Planck* sources within the extended HeViCS fields at 545 GHz. The list of sources can be found
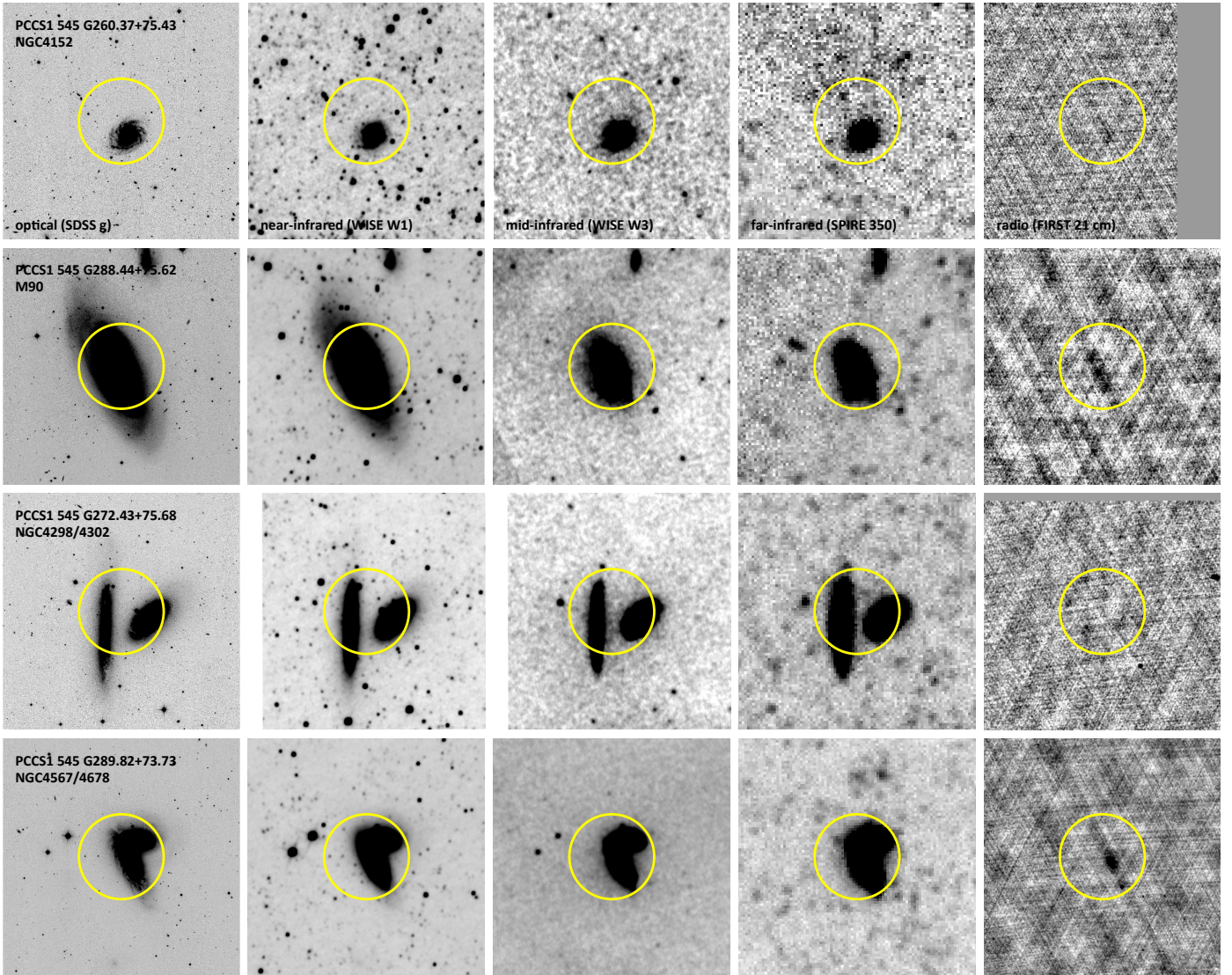
Fig. 1. Examples of *Planck* sources with an obvious counterpart at optical and infrared wavelengths. On each row, the different panels represent an optical *g*-band image from SDSS DR9 (Ahn et al. 2012), near- and mid-infrared images at 3.4 and 12 μm from the WISE survey (Wright et al. 2010), the *Herschel*/SPIRE 350 μm image from HeViCS, and a 20 cm radio continuum image from the VLA-FIRST radio survey (Becker et al. 1995). Each panel is 12×12 arcmin^2, and the yellow circle indicates the beam size of the HFI instrument at 857 GHz. The top two rows correspond to sources with individual Virgo Cluster galaxies as counterparts, the bottom two rows correspond to two pairs of Virgo Cluster galaxies.

in Table 2. The characterization of the sample is similar as for the 857 GHz sample: the vast majority (43 out of 48) of the *Planck* sources can be clearly identified with nearby galaxies. All of the 43 sources with clear optical counterparts are in common with the 857 GHz list, including the two galaxy pairs NGC 4298/4302 and NGC 4567/4568. All of the 545 GHz detected galaxies belong to the Virgo Cluster, i.e. the three background galaxies detected at 857 GHz are not detected anymore at 545 GHz.

Concerning the type of the galaxies detected, we note that the relative number of late-type galaxies has even increased compared to the 857 GHz detected population: more than half of all the galaxies detected at 545 GHz are of the Sc type. Remarkably fewer early-type spiral galaxies are detected: of the 10 Sa galaxies detected at 857 GHz, only one single system, NGC 4419, is also detected at 545 GHz. This galaxy at the centre of the Virgo Cluster is classified as a galaxy "at the end of the Sa sequence" (Sandage & Bedke 1994), and is characterized by an unusually high ratio between molecular versus atomic

gas (Kenney et al. 1990). Concerning the early-type galaxy population, we are left with only two galaxies: the synchrotron-dominated elliptical M 87, and the lenticular galaxy NGC 4526, known to host a prominent dust disc (Ferrarese et al. 2006; Sarzi et al. 2006; Young et al. 2009).

The PCCS contains five 545 GHz sources in the extended HeViCS fields without an obvious optical counterpart. Their nature will be discussed in Sect. 3.3.

3. Analysis and discussion

3.1. Flux density comparison

The *Planck* 857 GHz and SPIRE 350 μm filters were designed to have virtually the same transmission curve, with nearly identical central wavelength and bandwidth. Therefore, we can immediately compare the PCCS 857 GHz fluxes to the integrated SPIRE 350 μm fluxes, without significant color corrections.

SPIRE flux densities, both at 350 and 500 μm, are based on the results from Auld et al. (2013), who performed automated flux density determination of all Virgo Cluster VCC galaxies in the HeViCS fields. Their flux density determination method consists of several steps, including an advanced determination of the background, an iterative determination of the ideal aperture within which the flux is determined, and an elaborate determination of the uncertainty, taking into account contributions from calibration uncertainty, aperture uncertainty and zero-point uncertainty. The flux densities are presented in their Table B1. We have applied a number of additional corrections to these values. First, the fluxes were still based on the "old" SPIRE beam sizes, whereas these have been updated since. Secondly, Auld et al. (2013) did not contain a correction for extended fluxes, known as the K_{4E}/K_{4P} correction. And finally, the new SPIRE calibration, based on Neptune as a primary calibration source (Bendo et al. 2013), has been taken into account. The final correction factor comes down to a multiplication by a factor 0.90 and 0.87 at 350 and 500 μm, respectively. The final integrated flux densities we use for our comparison are listed in the last column of Tables 1 and 2 for 350 and 500 μm respectively.

As mentioned in Sect. 2.1, three galaxies detected at 857 GHz (IC 3029, NGC 4246 and NGC 4334) do not belong to the Virgo Cluster (even though they all have a number in the VCC). These background galaxies were not considered in Table B1 of Auld et al. (2013). For these galaxies, we have measured the SPIRE flux densities from the HeViCS maps using exactly the same technique.

Each source in the PCCS has four different measures of the flux density, depending on the source detection algorithm. The detection pipeline flux density (DETFLUX) is directly obtained from the filtered maps and assumes that the sources are point-like. The three other measures are estimated from the full-sky maps at the positions of the sources. The aperture photometry flux density (APERFLUX) is estimated by integrating the data in a circular aperture centred at the position of the source, with the average FWHM of the effective beam as radius for the aperture. The PSF fit photometry (PSFFLUX) is obtained by fitting a model of the PSF at the position of the source (Mitra et al. 2011). Finally, the Gaussian fit photometry flux density (GAUFLUX) is obtained by fitting a Gaussian model, centred at the position of the source, in which the size, shape and background offset are allowed to vary.

Planck Collaboration XXVIII. (2014) present a comparison between the different measures for the *Planck* PCCS 857 GHz flux densities and the SPIRE 350 μm flux densities for a set of galaxies from four different catalogues[1]. They found that, at low flux densities, the smallest dispersion between the SPIRE and *Planck* flux densities is achieved by the DETFLUX photometry because the filtering process removes structure not associated with compact sources. At the highest levels, corresponding to the most extended galaxies, the flux densities are underestimated by DETFLUX, APERFLUX and PSFFLUX. GAUFLUX accounts for the size of the source and is therefore able to estimate the flux density correctly. The general recommendation from the PCCS is that the appropriate photometry to be used depends on the nature of the source, with GAUFLUX to be used for the brightest

---

[1] Comparisons between SPIRE and *Planck* ERCSC fluxes have also been presented previously for individual galaxy samples, including the HeViCS Bright Galaxy Sample (Davies et al. 2012), the *Herschel* Reference Survey (Ciesla et al. 2012), and a sample of Planck-selected star forming galaxies (Negrello et al. 2013).

Table 3. Results of the linear regression fits of the SPIRE versus *Planck* flux densities.

Frequency	Flux density	a	b	$\chi^2_{\rm red}$
857 GHz	APERFLUX	0.944	0.0828	0.852
	DETFLUX	0.833	0.0953	1.643
	PSFFLUX	0.927	0.0723	1.778
	GAUFLUX	0.852	0.271	4.314
545 GHz	APERFLUX	0.884	0.0656	1.194
	DETFLUX	0.792	0.0262	1.431
	PSFFLUX	0.864	0.0483	1.968
	GAUFLUX	0.815	0.165	2.950

Notes. a and b represent the slope and intercept of the linear relation in the form $\log F_{Planck} = a \log F_{\rm SPIRE} + b$. The last column gives the reduced χ^2 value of the fit.

and most resolved sources. A similar conclusion was obtained by Herranz et al. (2013).

In Fig. 2 we show the comparison between the *Herschel* SPIRE 350 μm flux density and the *Planck* PCCS 857 GHz flux density, for each of the four different methods used in the PCCS to measure flux densities. The solid blue lines in the different panels correspond to a one-to-one correlation, the solid green lines represent a linear regression fit. These fits were made using the IDL MPFITEXY tool (Williams et al. 2010), based on the non-linear least-squares fitting package MPFIT (Markwardt 2009), and the parameters of these fits can be found in Table 3.

It is immediately obvious that the GAUFLUX is not an appropriate choice: only the highest flux densities at $S_{350} \gtrsim 10$ Jy are recovered fairly reliably, whereas lower flux densities are typically strongly overestimated. Somewhat surprisingly, the DETFLUX flux densities, which showed the smallest dispersion in the comparison of Planck Collaboration XXVIII. (2014), also show systematic deviations from the SPIRE flux densities. At high levels, the flux densities are systematically underestimated, as also found by Planck Collaboration XXVIII. (2014). Also at the lowest flux density levels, however, the DETFLUX measure shows a systematic overestimation compared to the SPIRE flux densities. This might be due to the flux boosting also noted by Herranz et al. (2013) for faint ERCSC sources in the H-ATLAS fields. We find the smallest scatter between the *Planck* and SPIRE flux densities for the APERFLUX flux density estimate. The flux densities agree very well, even up to the highest values where the DETFLUX estimate breaks down. The reduced χ^2 of this correlation is 0.852, which indicates that the error bars on the APERFLUX flux densities might be slightly overestimated. The PSFFLUX flux densities are a close second best, although the scatter at the lowest flux densities is a bit larger.

Comparing *Planck* 545 GHz and SPIRE 500 μm fluxes is less obvious, as the former filter has a significantly longer central wavelength (550 μm). In order to make a comparison possible, we converted the observed SPIRE 500 μm fluxes by multiplying it with a conversion factor. The FIR/submm SEDs of nearby galaxies in the Virgo Cluster can be approximated by a modified blackbody, $F_\nu \propto \nu^\beta B_\nu(T)$, with a temperature of $T \approx 20$ K and $\beta \approx 2$ (Davies et al. 2012; Auld et al. 2013). Taking into account the color corrections of the SPIRE 500 μm and *Planck* HFI 545 GHz bands, a color correction of 0.83 has to be applied to the SPIRE flux densities. A similar conversion factor (0.87) was obtained by Ciesla et al. (2012), based on a modified blackbody SED with $\beta = 1.5$. Only for M 87, for which the
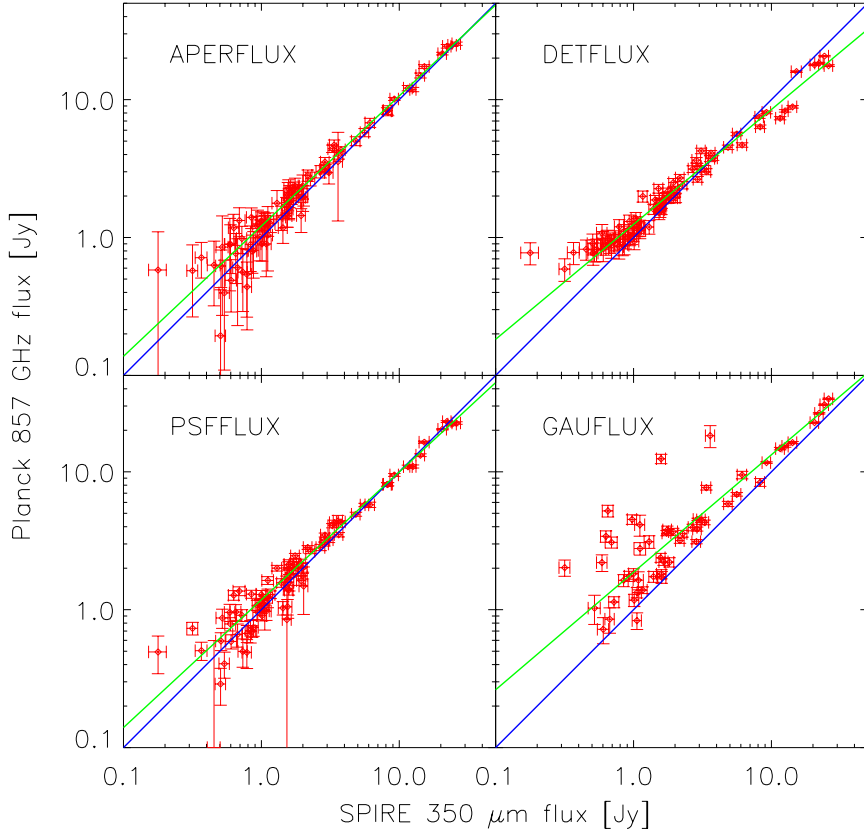
Fig. 2. Comparison between the *Herschel* SPIRE 350 μm flux density and the *Planck* 857 GHz flux density for the 82 PCCS sources with a clear counterpart. The different panels correspond to four different methods used in the PCCS to measure flux densities. The solid green line represents a linear regression fit to the data, the solid blue line corresponds to a one-to-one correlation. The GAUFLUX panel only contains 53 sources as this flux density estimate is not provided for all sources in the PCCS.

FIR/submm emission is completely dominated by synchrotron emission rather than by thermal dust emission (Shi et al. 2007; Baes et al. 2010), we applied a different conversion term. For a power-law synchrotron spectrum with $\alpha = -0.75$, we find a conversion term of 1.07.

The comparison between the observed *Planck* 550 μm flux densities and the converted SPIRE 500 μm flux densities is shown in Fig. 3, where each panel again corresponds to the different measures for the flux densities in the PCCS. The results of the linear regression fits can be found in Table 3. In general, we find the same behavior as for the comparison of the *Planck* 857 GHz and SPIRE 350 μm flux densities. For the highest flux density levels, DETFLUX and PSFFLUX underestimate the true flux densities, whereas GAUFLUX and APERFLUX do not suffer from this effect. Except for the brightest sources, the GAUFLUX estimates are the worst, with an exceptionally spurious flux density estimate more than an order of magnitude off for the otherwise unremarkable Sc galaxy NGC 4571. In general, the APERFLUX flux density estimates show least dispersion compared to the SPIRE flux densities. In this case, the PSFFLUX flux densities tend to underestimate the true flux densities significantly at the lowest levels.

3.2. Modified blackbody fits

The FIR/submm traced by *Herschel* and *Planck* is dominated by the emission from cold dust. The physical properties of the dust can in principle be determined by fitting SED models to the observed flux densities. While complex multi-component methods have been developed that take into account the entire range from mid-infrared to mm wavelengths (e.g., Draine & Li 2007; Compiègne et al. 2011; Galliano et al. 2011), the most common approach is a simple modified blackbody fit. This approach enables to determine the most fundamental properties of the dust medium: the mean dust temperature and the amount of dust.

In the Virgo Cluster, modified blackbody fits have been applied to the FIR/submm SED in several different studies: Davies et al. (2012) fitted modified blackbodies to a sample of SPIRE 500 μm selected galaxies, Auld et al. (2013) and Davies et al. (2013) used them to study the dust characteristics of a samples of optically selected galaxies, and Grossi et al. (2010), di Serego Alighieri et al. (2013) and De Looze et al. (2013) applied modified blackbody fits to smaller samples of star-forming dwarfs, early-type galaxies and transition-type galaxies, respectively. All of these studies relied on *Herschel* flux densities. One important question is whether the availability of additional *Planck* flux densities at 857 and 545 GHz substantially modifies the derived parameters.

In order to test this, we considered all galaxies in the HeViCS fields detected at 545 GHz, and constructed FIR/submm SEDs by combining the *Planck* HFI with *Herschel*/SPIRE observations at 250, 350 and 500 μm, *Herschel*/PACS data at 100 and 160 μm. The PACS and SPIRE fluxes and corresponding error bars were taken from Auld et al. (2013), where an automatic flux density measurement was applied to the five HeViCS maps for all galaxies from the Virgo Cluster Catalogue (Binggeli et al. 1985). Only M 87 was omitted from the sample as its SED is dominated by synchrotron emission rather than cold dust emission.
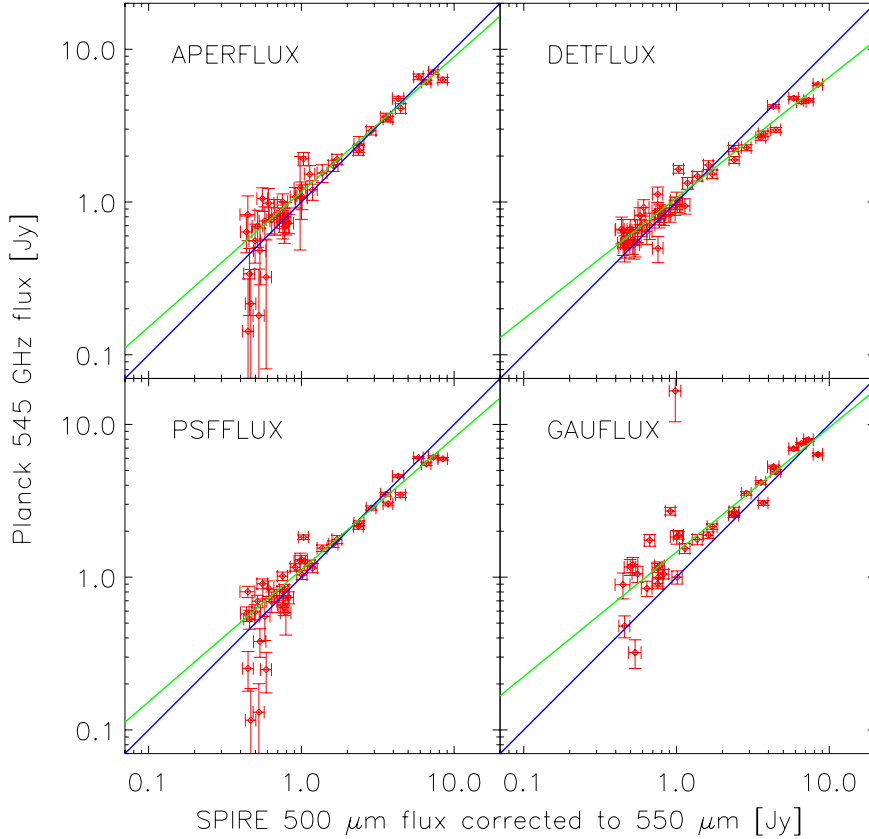
Fig. 3. Comparison between the *Herschel* SPIRE 500 μm flux density and the *Planck* 545 GHz flux density for the 43 PCCS sources with a clear counterpart. The *Herschel* flux densities have been converted to correspond to a wavelength of 550 μm (see text). The different panels correspond to four different methods used in the PCCS to measure flux densities. The solid green line represents a linear regression fit to the data, the solid blue line corresponds to a one-to-one correlation. The GAUFLUX panel only contains 33 sources as this flux density estimate is not provided for all sources in the PCCS.

We fitted the observed broadband fluxes using a simple modified blackbody function, i.e.

$$F_\nu = \frac{M_d}{D^2} \, \kappa_\nu \, B_\nu(T_d) \tag{1}$$

with M_d the dust mass, D the distance to the galaxy, T_d the dust temperature and κ_ν the emissivity. We used a common distance of 16.5 Mpc to all galaxies (Mei et al. 2007), and, as customary, we assume a power-law dust emissivity in the FIR/submm wavelength range, i.e. $\kappa_\nu \propto \nu^\beta$, where we fixed β to 1.8 (Planck Collaboration 2011i; Smith et al. 2013), and the zero-point to $\kappa_\nu = 0.192$ m^2 kg^{-1} at 350 μm (Draine 2003). Note that both the value of the emissivity index β and the absolute calibration of the emissivity are notoriously uncertain; actually, the quoted value of the zeropoint at $\lambda = 350\,\mu$m has been derived assuming a dust model with $\beta = 2$, so it would in principle not be applicable to models with a different value of β (for a discussion, see Bianchi 2013). However, the goal of the present exercise is not to determine absolute dust masses, but rather to compare SED fits with and without *Planck* data, so the absolute normalization of the emissivity (and the distance to the galaxies) is of less importance in our case. The two remaining free parameters in our fitting routine are the dust mass and the dust temperature. The fits were done by performing a χ^2 minimization using a simple gradient search method. Error bars on the derived parameters were derived using a Monte Carlo bootstrapping method.

Fitting modified blackbody fits to the PACS, SPIRE and HFI APERFLUX data, we find a mean temperature $\langle T_d \rangle = (21.3 \pm 3.2)$ K and dust mass $\langle \log M_d \rangle = 7.10 \pm 0.17$. These values are consistent with previous studies of the dust properties in late-type galaxies in the Virgo Cluster (Davies et al. 2012, 2013; Auld et al. 2013), especially if we take into account that sometimes other assumptions have been made on the value of β and the distances. More important here than the absolute values, however, is whether the inclusion of *Planck* data has a systematic effect on the derived dust characteristics. Figure 4 compares the dust mass and temperature for all galaxies in our sample, fitted with and without the *Planck* 857 and 545 GHz flux densities. The consistency between both fits is convincing: for every individual galaxy in our sample, the fitted modified blackbody parameters are fully consistent within the error bars. This implies that the addition or omission of the *Planck* 857 and 545 GHz flux densities does not imply a systematic bias, which is not unexpected given the good agreement between the SPIRE and *Planck* HFI flux densities (Sect. 3.1).

Note that we have, at this stage, limited ourselves to the 857 and 545 GHz data, whereas *Planck* covers wavelengths up to the mm range. Our conclusion that the addition of 857 and 545 GHz data to the *Herschel* PACS and SPIRE data points does not affect the derived dust parameters does not necessarily imply that the same applies when longer wavelength *Planck* data are also taken into account. In particular, there has been quite some evidence for a submm/mm excess beyond a simple modified blackbody, in particular for dwarf galaxies (e.g., Galliano et al. 2003, 2005, 2011; Galametz et al. 2009, 2011; Israel et al. 2010; Planck Collaboration 2011f; Dale et al. 2012). A study of the population of *Planck* sources detected at longer wavelengths, including their extended spectral energy distribution, the implied dust
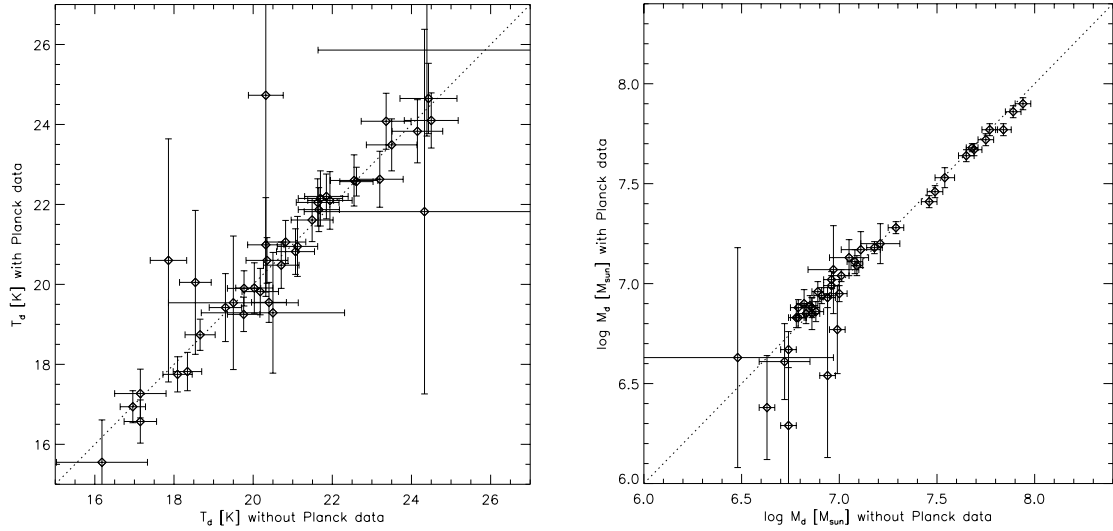
Fig. 4. Comparison between the dust temperature and dust mass of 42 Virgo Cluster galaxies detected by *Planck* at 545 GHz, as derived from modified blackbody fits to the *Herschel* data alone (horizontal axis) and the combined *Herschel* and *Planck* 857 and 545 data (vertical axis). The dotted line corresponds to a one-to-one relation.

properties and a possible submm/mm excess, will be considered in a separate HeViCS study.

3.3. Nature of the sources without counterparts

The PCCS contains two 857 GHz sources and five 545 GHz sources without an obvious nearby galaxy as counterpart. These *Planck* sources are particularly interesting as their submm flux density might originate from the common contribution of intermediate redshift galaxies or high-redshift ultra-luminous infrared galaxies. An example of such a compact 857 GHz *Planck* source is PLCKERC857 G270.59+58.52, linked to the strongly lensed hyperluminous starburst galaxy H-ATLAS J114637.9+001132 (Fu et al. 2012).

Within the beam area around the position of the first unidentified 857 GHz source in the HeViCS fields, PCCS1 857 G261.44+74.24, NED lists 55 SDSS galaxies and one NVSS radio source. All of these galaxies are very dim at optical wavelengths: one galaxy has a g-band magnitude of 15.8, the others all are fainter than $m_g = 17.7$ mag. The top panel of Fig. 5 compares the HeViCS SPIRE 350 μm image of the region around PCCS1 857 G261.44+74.24 with an optical SDSS image, near- and mid-infrared images from WISE and a radio continuum image from FIRST. The SPIRE image contains a number of discrete sources, all of them with flux densities below 75 mJy. Only one of the sources, with $S_{350} \sim 40$ mJy, has an obvious galaxy as counterpart in the SDSS map, the $m_g = 17.7$ mag galaxy SDSS J120835+145750 at redshift $z = 0.083$. This *Planck* source is located at the edge of a prominent cirrus feature that extends from the centre of the cluster in the northwestern direction (Fig. 6), and it is marked as an extended source in the PCCS, i.e. it has the EXTENDED flag equal to one. Putting all this information together, it seems logical that the *Planck* detection corresponds to a Galactic cirrus feature (with potentially a non-negligible contribution from background galaxies).

The second unidentified 857 GHz PCCS source, PCCS1 857 G270.81+76.99 (Fig. 5, second row), is located in a region less affected by Galactic cirrus and is not marked as an extended source in the PCCS. NED lists 37 sources with the beam centered around the position of the source, most of them

SDSS galaxies fainter than $m_g = 19$ mag. This might hence be a more promising candidate for an intermediate or high-redshift counterpart. However, the source is located very close (<3 arcmin) to M100, with a flux density of almost 26 Jy the brightest source in the Virgo Cluster at 350 μm (Auld et al. 2013). As there are no SPIRE 350 μm sources with flux densities above 50 mJy within the *Planck* beam at this position (second row in Fig. 5), we presume that this source is a spurious detection.

The five 545 GHz PCCS sources without obvious optical counterpart are different from the two 857 GHz sources without optical counterpart. Looking at the position of these sources on the HeViCS map (Fig. 6), it seems obvious for at least two sources (PCCS1 545 G287.49+72.83 and G286.36+76.69) that they are associated with Galactic cirrus emission, as they are located on top of the notorious Galactic cirrus ring that surrounds the central regions of the Virgo Cluster (e.g., Mihos et al. 2005; Rudick et al. 2010; Cortese et al. 2010a). Also for the other sources, we expect them to be dominated by cirrus emission. In all cases, the corresponding fields in the HeViCS SPIRE maps show a collection of faint sources, none of them bright enough to contribute a substantial part of the submm flux density, and most of them not associated to obvious sources in the corresponding SDSS optical maps (bottom two rows of Fig. 5).

Altogether, the number of PCCS sources without optical counterpart is very modest, especially at 857 GHz (2 out of 84). This is particularly striking when we compare these numbers to the results from the equatorial fields of the H-ATLAS survey by Herranz et al. (2013). Of the 28 *Planck* sources they found at 857 GHz, only 11 correspond to bright low-redshift galaxies (one of them a pair of nearby galaxies) and as many as 17 have no nearby galaxy as counterpart. Of these 17 unidentified sources, one source is resolved into a condensation of high-redshift point sources clustered around a strongly lensed galaxy, while the remaining 16 are probably related to Galactic cirrus features. A similar situation, but with fewer detected sources, is seen at 545 GHz.

Even though it is logical that we detect many more nearby galaxies compared to Herranz et al. (2013) (as we are looking at a nearby cluster), the number of sources without optical
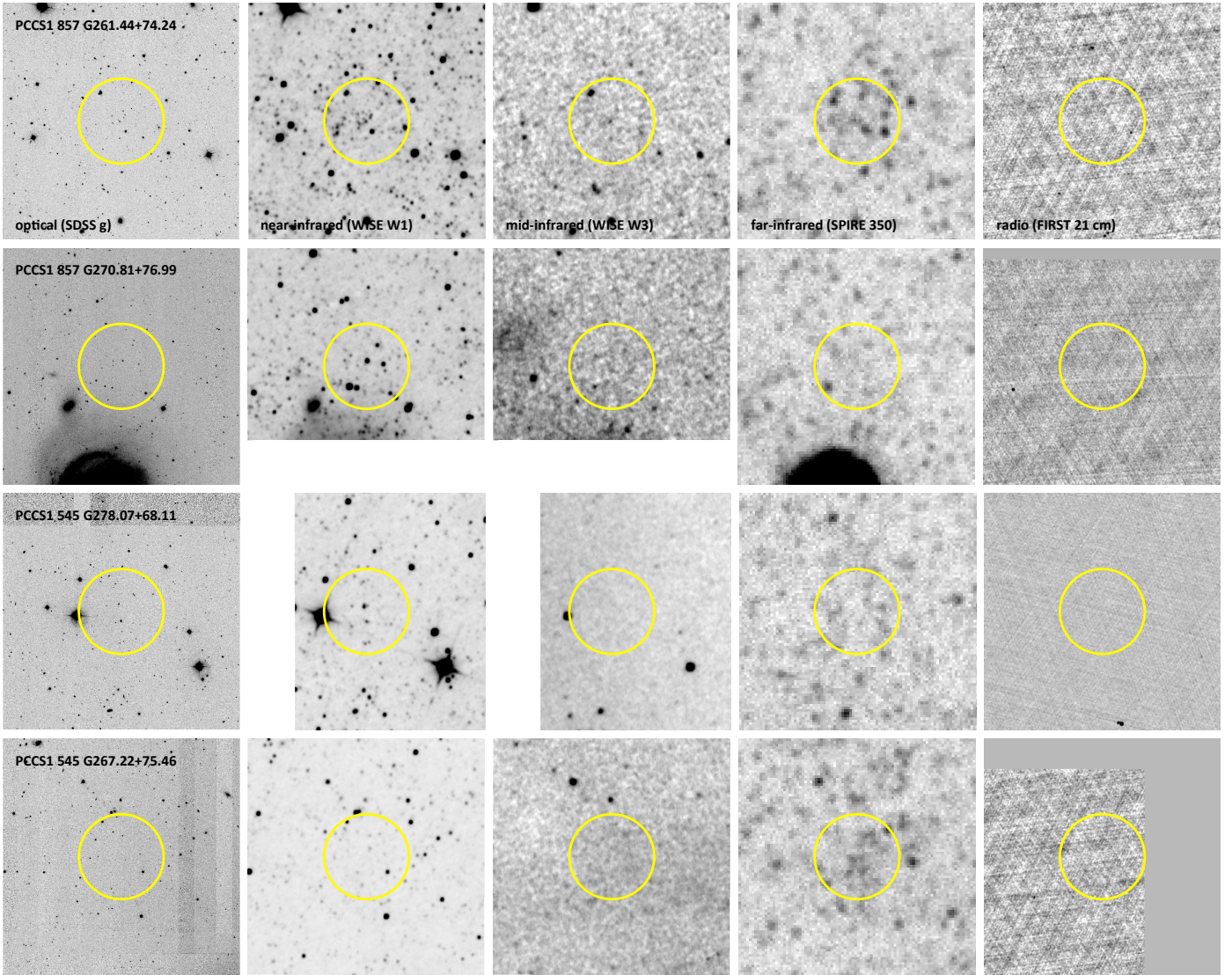
Fig. 5. Same as Fig. 1, but now for four *Planck* sources without an obvious counterpart at optical wavelengths or on the *Herschel* maps.

counterpart remains modest. Based on the number of sources and the area of the H-ATLAS equatorial fields (134.55 deg^2), we would expect 10 to 11 sources at 857 GHz without obvious optical counterpart. The obvious reason that explains this difference is the high Galactic latitude ($b = 67-76$ deg) of the HeViCS fields compared to the equatorial H-ATLAS fields. In particular, all but one of the *Planck* detections by Herranz et al. (2013) are located in the GAMA-09 field, located at a Galactic latitude around 30 deg and known to be strongly contaminated by cirrus (Bracco et al. 2011). In spite of the clear signatures of cirrus in the HeViCS fields (see Fig. 6), this difference in Galactic latitude is probably responsible for the much lower number of *Planck* cirrus features. An additional factor could have been the difference between the *Planck* catalogues used for both studies: we use the PCCS, whereas Herranz et al. (2013) use the ERCSC. Compared to the ERCSC, the PCCS uses a different extraction method that is better at excluding slightly extended objects.

Finally, we did not find any *Planck* source in the HeViCS fields that corresponds to a proto-cluster of intermediate or high-redshift dusty galaxies or strongly lensed submm sources. Based on the extrapolation of the Herranz et al. (2013) results, at most one such source would be expected. One factor to take into account is again the source extraction method used by PCCS, which is better at excluding slightly extended objects (not only cirrus, but also high-redshift clumps).

We can also attempt to make an estimate based on theoretical studies whether it is expected that no high-redshift *Planck* sources are detected in the HeViCS fields. Negrello et al. (2005) made predictions on the surface density of proto-clusters of dusty galaxies detectable by *Planck*. For the evolution indicated by simulations, they expect a surface density at the *Planck* detection limit below 10^{-2} deg^{-2}. This corresponds to at most one detected proto-cluster in the HeViCS fields. These predictions are, however, endowed with very large uncertainties both because the predicted counts of proto-clusters are very steep (and therefore are critically dependent on the detection limit which is hard to determine because the protoclusters are expected to be resolved by *Planck*), and because there is a considerable uncertainty on the evolution of key quantities such as the amplitude of the three-point correlation function. It is expected that, for luminous matter, this amplitude behaves as b^{-1} or b^{-2}, where b is the bias parameter (Fry & Gaztanaga 1993; Szapudi et al. 2001), and in this case the expected surface density decreases by more than an order of magnitude compared to the case without three-point correlation amplitude redshift evolution. Moreover, due to
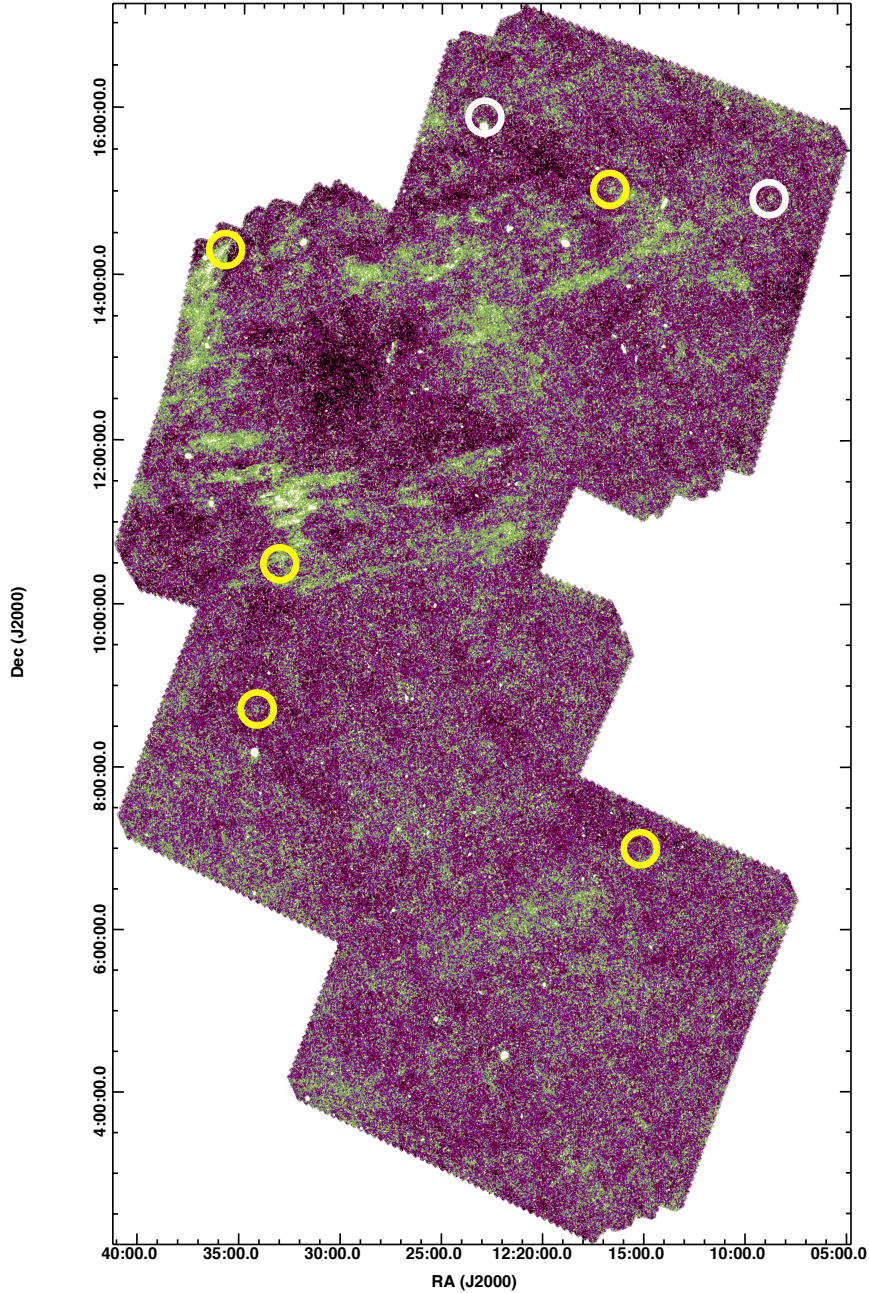
Fig. 6. Location of the PCCS sources without obvious SDSS or HeViCS counterpart on the HeViCS SPIRE 350 μm map. The white circles correspond to the 857 GHz sources, the yellow circles to 545 GHz sources. The SPIRE map has been smoothed to enhance the visibility of the Galactic cirrus features.

the relatively small field size and the effect of cosmic variance, it is difficult to make a firm estimate of the expected number of sources. On the other hand, the expected number counts of the sources as a function of flux density are quite steep (Negrello et al. 2005), so it is likely that substantially more submm bright proto-clusters can be found at fainter fluxes.

Negrello et al. (2007) and Lapi et al. (2012) present predictions of the surface density of lensed spheroids. Constrained by the number of detected and candidate strongly lensed submm galaxies in the H-ATLAS Science Demonstration Field (Negrello et al. 2010; González-Nuevo et al. 2012), the models of Lapi et al. (2012) predict a surface density around 8 × 10^{-4} deg^{-2} at a 500 μm flux density limit of 1 Jy. Again, this estimation is very uncertain and could in principle be considered

as a lower limit, as the number of lensed spheroids decreases very quickly with flux density and the well-known clustering of submm sources (Maddox et al. 2010; Short & Coles 2011; van Kampen et al. 2012) is not taken into account in these estimates. In any case, these numbers are so low that we do not expect any high-z lensed systems in the 84 deg^2 HeViCS fields above the *Planck* detection limit.

3.4. Completeness and positional accuracy of the PCCS

According to Planck Collaboration XXVIII. (2014), the PCCS catalogue should be 90% complete at 857 GHz down to a flux density level of 680 mJy. To verify this, we checked the SPIRE 350 μm flux densities of all Virgo Cluster galaxies

in the catalogue of Auld et al. (2013). This catalogue contains 72 galaxies with a $S_{350} > 680$ mJy (taking into account the correction factors for the old beam size, extended flux density correction and updated SPIRE calibration). Sixty-nine of these sources are detected by *Planck* in the PCCS (as 67 sources, as two pairs of galaxies are blended into single *Planck* sources). The three non-detected sources (IC 3061, NGC 4351, and NGC 4435) all have SPIRE 350 μm flux densities below 720 mJy. Below $S_{350} \sim 650$ mJy the detection rate drops quickly, although there are still occasional PCCS detections with even lower SPIRE flux densities. The most extreme case is the peculiar Sa galaxy NGC 4506 with $S_{350} = 178$ mJy, which stands out in Fig. 2 as the isolated point at the extreme left of the panels. Flux boosting and confusion with Galactic cirrus emission are probably responsible for the fact that this galaxy made it to the PCCS: it is located on top of the previously mentioned prominent cirrus ring in the centre of the Virgo Cluster.

The PCCS 545 GHz catalogue is reported to have a 90% completeness limit of 570 mJy (Planck Collaboration XXVIII. 2014). Using the conversion factor 0.83 as derived in Sect. 3, this corresponds to a 500 μm flux density level of 687 mJy. There are 37 galaxies in the Auld et al. (2013) catalogue with a SPIRE 500 μm flux density above 687 mJy (again taking into account the previously mentioned correction factors). All but one of these sources, the edge-on spiral NGC 4316 with $S_{500} = 694$ mJy, are detected by *Planck* at 545 GHz. The faintest source detected has $S_{500} = 502$ mJy.

Overall, our results are in good agreement with the PCCS completeness estimates: in the HeViCS fields, the PCCS recovered ~95% of the sources with $S_{350} > 680$ mJy and ~95% of the sources with $S_{550} > 570$ mJy. This is the first empirical confirmation of the estimated completeness of the PCCS. For the HFI bands, the PCCS completeness estimates were based on simulations in which unresolved point sources of different intrinsic flux density levels were injected in the real maps and convolved with the effective beam. The fact that we confirm these numbers is a strong support for the internal PCCS validation procedure.

Finally, in order to test the positional accuracy of the PCCS, we checked the positions of the sources as listed in the PCCS catalogue (and listed in Tables 1 and 2) with the central positions of the galaxies obtained from NED. The results are shown in Fig. 7. There is no systematic offset, and the general positional accuracy is 0.71 ± 0.29 arcmin for the 857 GHz band, and 0.79 ± 0.36 arcmin for the 545 GHz band. These numbers are some 10% larger than, but still fully consistent with, the positional uncertainties quoted by (Planck Collaboration XXVIII. 2014) based on the PCCS sources from the KINGFISH, HRS, H-ATLAS and HeViCS BGS samples (0.65 at 857 GHz and 0.72 at 545 GHz).

4. Conclusion and summary

We have cross-correlated the *Planck* Catalogue of Compact Sources (PCCS) with the 84 deg² survey fields of the *Herschel* Virgo Cluster Survey (HeViCS), with the goals of identifying and characterizing the counterparts of the compact *Planck* sources at 857 and 545 GHz, and searching for possible high-redshift gravitational lenses or proto-clusters of star-forming galaxies. The results of this investigation are the following:

1. We find 84 compact *Planck* sources at 857 GHz in the HeViCS survey fields; 77 of these sources correspond
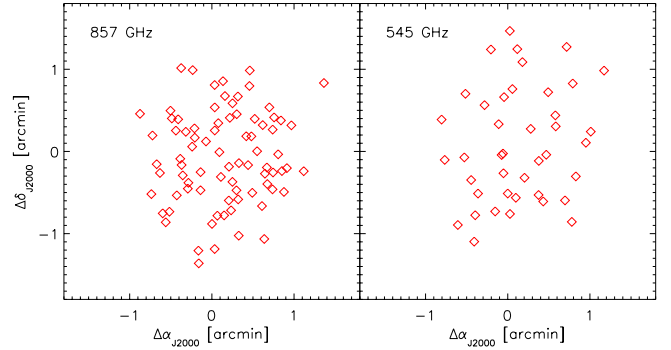

Fig. 7. Positional accuracy of the PCCS at 857 GHz (*left panel*) and 545 GHz (*right panel*). The plots show the difference in right ascension and declination between the position of the PCCS source and the coordinates of the centre of the optical counterpart, for all sources with a single nearby galaxy as counterpart.

to individual Virgo Cluster galaxies, 3 to nearby background galaxies, and 2 to galaxy pairs in the Virgo Cluster. Only 2 sources do not have a clearly identifiable counterpart at optical and FIR/submm wavelengths.

2. At 545 GHz, where the dominant emission mechanism is still continuum emission by cold and large dust grains, we find 48 sources in the PCCS; 41 of these sources have a single Virgo Cluster galaxy as counterpart, two correspond to a Virgo Cluster galaxy pair, and 5 sources have no nearby galaxy as a clearly identifiable counterpart at optical or submm wavelengths. No background galaxies are detected, and all sources with a counterpart, including the two galaxy pairs, are also detected at 857 GHz.

3. The vast majority of all *Planck* detected galaxies are late-type spiral galaxies, with the Sc class dominating the numbers (more than half of all galaxies detected at 545 GHz). The number of early-type spirals reduces sharply when moving from 857 to 545 GHz: of the 43 galaxies detected at 545 GHz, there is only one Sa galaxy, compared to 10 out of 82 at the 857 GHz. Early-type galaxies are virtually absent from the PCCS, with only three lenticular galaxies (NGC 4370, 4429 and 4526) and one elliptical galaxy (M 87) detected. In the latter galaxy, detected at both 857 and 545 GHz, the submm emission is dominated by synchrotron rather than dust emission.

4. The PCCS presents four different estimates for the flux density, reflecting the different methods used to detect sources and measure their flux density. We have compared these different flux density measures to the SPIRE 350 and 500 μm flux density measures from the HeViCS Virgo Cluster catalogue (Auld et al. 2013). The *Planck* pipeline source detection algorithm estimate, DETFLUX, which showed the smallest dispersion in the comparison of Planck Collaboration XXVII. (2014), shows systematic deviations both at the highest and the lowest flux densities. We find the best correlation between the SPIRE flux densities and the *Planck* aperture photometry flux densities (APERFLUX), even at the highest flux density levels. At 857 GHz, a linear regression fit results in a reduced χ^2 compatible with a relation without intrinsic scatter.

5. Based on the number of detected Virgo Cluster galaxies, we have estimated the completeness and positional accuracy of the PCCS at 857 and 545 GHz. Our estimates are in agreement with the results from Planck Collaboration XXVIII. (2014), who report 90% complete-

ness limits of 680 and 570 mJy at 857 and 545 GHz respectively. Our study is the first empirical confirmation of the claimed completeness of the PCCS at submm wavelengths, which was estimated based on simulations, and hence provides a strong support for the internal PCCS validation procedure.

6. We have found only seven PCCS sources in the HeViCS fields without a nearby galaxy as obvious counterpart (two sources at 857 GHz and five sources at 545 GHz). Based on their location in the cluster and the SDSS and HeViCS sources at their positions, we conclude that all of these are probably linked to Galactic cirrus features or spurious detections. The number of sources without counterpart is remarkably low compared to the study by Herranz et al. (2013), who found that more than half of the compact *Planck* sources in the H-ATLAS equatorial fields correspond to cirrus features. This might be due to a combination of the higher galactic latitude of the Virgo Cluster compared to the equatorial H-ATLAS fields and the different *Planck* catalogue used. Unlike Herranz et al. (2013), we find no *Planck* sources in the HeViCS fields associated to high-redshift proto-clusters of dusty galaxies or strongly lensed submm sources.

References

Ahn, C. P., Alexandroff, R., Allende Prieto, C., et al. 2012, ApJS, 203, 21
Auld, R., Bianchi, S., Smith, M. W. L., et al. 2013, MNRAS, 428, 1880

Baes, M., Clemens, M., Xilouris, E. M., et al. 2010, A&A, 518, L53
Becker, R. H., White, R. L., & Helfand, D. J. 1995, ApJ, 450, 559
Bendo, G. J., Wilson, C. D., Pohlen, M., et al. 2010, A&A, 518, L65
Bendo, G. J., Boselli, A., Dariush, A., et al. 2012, MNRAS, 419, 1833
Bendo, G. J., Griffin, M. J., Bock, J. J., et al. 2013, MNRAS, 433, 3062
Bersanelli, M., Mandolesi, N., Butler, R. C., et al. 2010, A&A, 520, A4
Bianchi, S. 2013, A&A, 552, A89
Binggeli, B., Sandage, A., & Tammann, G. A. 1985, AJ, 90, 1681
Böhringer, H., Briel, U. G., Schwarz, R. A., et al. 1994, Nature, 368, 828
Boquien, M., Calzetti, D., Combes, F., et al. 2011, AJ, 142, 111
Boselli, A., Ciesla, L., Buat, V., et al. 2010a, A&A, 518, L61
Boselli, A., Eales, S., Cortese, L., et al. 2010b, PASP, 122, 261
Boselli, A., Boissier, S., Heinis, S., et al. 2011, A&A, 528, A107
Boselli, A., Ciesla, L., Cortese, L., et al. 2012, A&A, 540, A54
Bracco, A., Cooray, A., Veneziani, M., et al. 2011, MNRAS, 412, 1151
Buson, L., Bressan, A., Panuzzo, P., et al. 2009, ApJ, 705, 356
Ciesla, L., Boselli, A., Smith, M. W. L., et al. 2012, A&A, 543, A161
Clemens, M. S., Negrello, M., De Zotti, G., et al. 2013, MNRAS, 433, 695
Clements, D. L., Rigby, E., Maddox, S., et al. 2010, A&A, 518, L8
Compiègne, M., Verstraete, L., Jones, A., et al. 2011, A&A, 525, A103
Corbelli, E., Bianchi, S., Cortese, L., et al. 2012, A&A, 542, A32
Cortese, L., Bendo, G. J., Isaak, K. G., Davies, J. I., & Kent, B. R. 2010a, MNRAS, 403, L26
Cortese, L., Davies, J. I., Pohlen, M., et al. 2010b, A&A, 518, L49
Cotton, W. D., Mason, B. S., Dicker, S. R., et al. 2009, ApJ, 701, 1872
Dale, D. A., Aniano, G., Engelbracht, C. W., et al. 2012, ApJ, 745, 95
Davies, J., Minchin, R., Sabatini, S., et al. 2004, MNRAS, 349, 922
Davies, J. I., Baes, M., Bendo, G. J., et al. 2010, A&A, 518, L48
Davies, J. I., Bianchi, S., Cortese, L., et al. 2012, MNRAS, 419, 3505
Davies, J. I., Bianchi, S., Baes, M., et al. 2013, MNRAS, in press [arXiv:1311.1774]
de Graauw, T., Helmich, F. P., Phillips, T. G., et al. 2010, A&A, 518, L6
De Looze, I., Baes, M., Zibetti, S., et al. 2010, A&A, 518, L54
De Looze, I., Baes, M., Boselli, A., et al. 2013, MNRAS, 436, 1057
de Vaucouleurs, G., de Vaucouleurs, A., Corwin, Jr., H. G., et al. 1991, Third Reference Catalogue of Bright Galaxies (New York: Springer)
di Serego Alighieri, S., Bianchi, S., Pappalardo, C., et al. 2013, A&A, 552, A8
Draine, B. T. 2003, ARA&A, 41, 241
Draine, B. T., & Li, A. 2007, ApJ, 657, 810
Eales, S., Dunne, L., Clements, D., et al. 2010, PASP, 122, 499
Ferrarese, L., Côté, P., Jordán, A., et al. 2006, ApJS, 164, 334
Ferrarese, L., Côté, P., Cuillandre, J.-C., et al. 2012, ApJS, 200, 4
Fry, J. N., & Gaztanaga, E. 1993, ApJ, 413, 447
Fu, H., Jullo, E., Cooray, A., et al. 2012, ApJ, 753, 134
Galametz, M., Madden, S., Galliano, F., et al. 2009, A&A, 508, 645
Galametz, M., Madden, S. C., Galliano, F., et al. 2011, A&A, 532, A56
Galliano, F., Madden, S. C., Jones, A. P., et al. 2003, A&A, 407, 159
Galliano, F., Madden, S. C., Jones, A. P., Wilson, C. D., & Bernard, J.-P. 2005, A&A, 434, 867
Galliano, F., Hony, S., Bernard, J.-P., et al. 2011, A&A, 536, A88
Gavazzi, G., Boselli, A., Donati, A., Franzetti, P., & Scodeggio, M. 2003, A&A, 400, 451
González-Nuevo, J., Lapi, A., Fleuren, S., et al. 2012, ApJ, 749, 65
Griffin, M. J., Abergel, A., Abreu, A., et al. 2010, A&A, 518, L3
Grossi, M., Hunt, L. K., Madden, S., et al. 2010, A&A, 518, L52
Harris, A. I., Baker, A. J., Frayer, D. T., et al. 2012, ApJ, 752, 152
Hartogh, P., Lis, D. C., Bockelée-Morvan, D., et al. 2011, Nature, 478, 218
Herranz, D., González-Nuevo, J., Clements, D. L., et al. 2013, A&A, 549, A31
Holland, W. S., Robson, E. I., Gear, W. K., et al. 1999, MNRAS, 303, 659
Holland, W., MacIntosh, M., Fairley, A., et al. 2006, in Proc. SPIE, 6275, 1E
Israel, F. P., Wall, W. F., Raban, D., et al. 2010, A&A, 519, A67
Kenney, J. D. P., Young, J. S., Hasegawa, T., & Nakai, N. 1990, ApJ, 353, 460
Kennicutt, R. C., Calzetti, D., Aniano, G., et al. 2011, PASP, 123, 1347
Kessler, M. F., Steinz, J. A., Anderegg, M. E., et al. 1996, A&A, 315, L27
Lamarre, J.-M., Puget, J.-L., Ade, P. A. R., et al. 2010, A&A, 520, A9
Lapi, A., González-Nuevo, J., Fan, L., et al. 2011, ApJ, 742, 24
Lapi, A., Negrello, M., González-Nuevo, J., et al. 2012, ApJ, 755, 46
Lawrence, A., Warren, S. J., Almaini, O., et al. 2007, MNRAS, 379, 1599
Maddox, S. J., Dunne, L., Rigby, E., et al. 2010, A&A, 518, L11
Magrini, L., Bianchi, S., Corbelli, E., et al. 2011, A&A, 535, A13
Markwardt, C. B. 2009, in Astronomical Data Analysis Software and Systems XVIII, eds. D. A. Bohlender, D. Durand, & P. Dowler, ASP Conf. Ser., 411, 251
Mei, S., Blakeslee, J. P., Côté, P., et al. 2007, ApJ, 655, 144
Mihos, J. C., Harding, P., Feldmeier, J., & Morrison, H. 2005, ApJ, 631, L41
Mitra, S., Rocha, G., Górski, K. M., et al. 2011, ApJS, 193, 5
Mould, J. R., Huchra, J. P., Freedman, W. L., et al. 2000, ApJ, 529, 786
Müller, T. G., Lellouch, E., Stansberry, J., et al. 2010, A&A, 518, L146

Murakami, H., Baba, H., Barthel, P., et al. 2007, PASJ, 59, 369
Negrello, M., González-Nuevo, J., Magliocchetti, M., et al. 2005, MNRAS, 358, 869
Negrello, M., Perrotta, F., González-Nuevo, J., et al. 2007, MNRAS, 377, 1557
Negrello, M., Hopwood, R., De Zotti, G., et al. 2010, Science, 330, 800
Negrello, M., Clemens, M., Gonzalez-Nuevo, J., et al. 2013, MNRAS, 429, 1309
Neugebauer, G., Habing, H. J., van Duinen, R., et al. 1984, ApJ, 278, L1
Oliver, S. J., Bock, J., Altieri, B., et al. 2012, MNRAS, 424, 1614
Pascale, E., Ade, P. A. R., Bock, J. J., et al. 2008, ApJ, 681, 400
Pilbratt, G. L., Riedinger, J. R., Passvogel, T., et al. 2010, A&A, 518, L1
Planck Collaboration 2011a, A&A, 536, A1
Planck Collaboration 2011b, A&A, 536, A7
Planck Collaboration 2011c, A&A, 536, A19
Planck Collaboration 2011d, A&A, 536, A15
Planck Collaboration 2011e, A&A, 536, A16
Planck Collaboration 2011f, A&A, 536, A17
Planck Collaboration 2011g, A&A, 536, A21
Planck Collaboration 2011h, A&A, 536, A22
Planck Collaboration 2011i, A&A, 536, A25
Planck Collaboration I. 2014, A&A, in press [arXiv:1303.5062]
Planck Collaboration XV. 2014, A&A, in press [arXiv:1303.5075]
Planck Collaboration XVI. 2014, A&A, in press [arXiv:1303.5076]

Planck Collaboration XXVIII. 2014, A&A, in press [arXiv:1303.5088]
Poglitsch, A., Waelkens, C., Geis, N., et al. 2010, A&A, 518, L2
Rudick, C. S., Mihos, J. C., Harding, P., et al. 2010, ApJ, 720, 569
Sandage, A., & Bedke, J. 1994, The Carnegie Atlas of Galaxies (Carnegie Institution of Washington Publ.)
Sarzi, M., Falcón-Barroso, J., Davies, R. L., et al. 2006, MNRAS, 366, 1151
Shi, Y., Rieke, G. H., Hines, D. C., Gordon, K. D., & Egami, E. 2007, ApJ, 655, 781
Short, J., & Coles, P. 2011, MNRAS, 412, L93
Siringo, G., Kreysa, E., Kovács, A., et al. 2009, A&A, 497, 945
Smith, D. J. B., Hardcastle, M. J., Jarvis, M. J., et al. 2013, MNRAS, 436, 2435
Smith, M. W. L., Vlahakis, C., Baes, M., et al. 2010, A&A, 518, L51
Springob, C. M., Haynes, M. P., Giovanelli, R., & Kent, B. R. 2005, ApJS, 160, 149
Springob, C. M., Masters, K. L., Haynes, M. P., Giovanelli, R., & Marinoni, C. 2009, ApJS, 182, 474
Szapudi, I., Postman, M., Lauer, T. R., & Oegerle, W. 2001, ApJ, 548, 114
Thacker, C., Cooray, A., Smidt, J., et al. 2013, ApJ, 768, 58
van Kampen, E., Smith, D. J. B., Maddox, S., et al. 2012, MNRAS, 426, 3455
Werner, M. W., Roellig, T. L., Low, F. J., et al. 2004, ApJS, 154, 1
Williams, M. J., Bureau, M., & Cappellari, M. 2010, MNRAS, 409, 1330
Wright, E. L., Eisenhardt, P. R. M., Mainzer, A. K., et al. 2010, AJ, 140, 1868
Young, L. M., Bendo, G. J., & Lucero, D. M. 2009, AJ, 137, 3053

Table 1. *Planck* 857 GHz PCCS sources in the extended HeViCS survey area.

PCCS source	α_{J2000} (deg)	δ_{J2000} (deg)	PCCS 857 GHz (Jy)	Counterpart	VCC	Type	SPIRE 350 μm (Jy)
PCCS1 857 G261.44+74.24	182.12855	14.94011	0.746 ± 0.136	· · ·	· · ·	· · ·	· · ·
PCCS1 857 G260.38+75.42	182.66101	16.03927	2.111 ± 0.147	NGC 4152	25	Sc	1.996 ± 0.149
PCCS1 857 G266.31+73.24	182.68154	13.34018	0.591 ± 0.110	IC 3029	27	Sc	0.317 ± 0.029
PCCS1 857 G269.69+72.43	183.12050	12.12778	0.980 ± 0.154	IC 769	58	Sb	0.877 ± 0.072
PCCS1 857 G276.80+67.94	183.26859	07.04378	1.770 ± 0.158	NGC 4180	73	Sb	1.582 ± 0.114
PCCS1 857 G268.39+73.70	183.44470	13.41055	3.140 ± 0.175	NGC 4189	89	Sc	2.687 ± 0.196
PCCS1 857 G265.42+74.97	183.46055	14.91470	7.332 ± 0.194	M 98	92	Sb	11.571 ± 0.840
PCCS1 857 G268.93+73.52	183.48450	13.17543	1.610 ± 0.144	NGC 4193	97	Sc	1.592 ± 0.125
PCCS1 857 G278.93+66.94	183.64987	05.81024	1.749 ± 0.129	NGC 4197	120	Scd	1.574 ± 0.118
PCCS1 857 G270.21+73.54	183.81944	13.01505	1.942 ± 0.151	NGC 4206	145	Sc	2.205 ± 0.149
PCCS1 857 G268.89+74.36	183.91888	13.90904	4.512 ± 0.168	NGC 4212	157	Sc	4.847 ± 0.346
PCCS1 857 G270.46+73.72	183.97418	13.13815	8.083 ± 0.188	NGC 4216	167	Sb	9.207 ± 0.656
PCCS1 857 G270.58+73.91	184.10005	13.29014	1.586 ± 0.188	NGC 4222	187	Scd	1.559 ± 0.115
PCCS1 857 G267.17+75.77	184.29755	15.33868	2.645 ± 0.129	NGC 4237	226	Sc	2.919 ± 0.210
PCCS1 857 G282.23+65.16	184.30274	03.67542	0.878 ± 0.129	NGC 4234	221	Sc	0.857 ± 0.068
PCCS1 857 G279.82+68.01	184.35336	06.68030	0.814 ± 0.149	NGC 4223	234	Sa	0.521 ± 0.052
PCCS1 857 G279.69+68.53	184.49064	07.18604	1.055 ± 0.124	NGC 4246	264	Sc	1.000 ± 0.079
PCCS1 857 G270.45+75.20	184.71895	14.42515	20.680 ± 0.251	M 99	307	Sc	24.229 ± 1.720
PCCS1 857 G282.51+66.97	184.98252	05.35636	3.772 ± 0.146	NGC 4273	382	Sc	3.776 ± 0.277
PCCS1 857 G280.56+69.18	185.01716	07.68557	0.985 ± 0.144	NGC 4276	393	Sc	0.651 ± 0.059
PCCS1 857 G284.34+65.49	185.24478	03.73035	1.156 ± 0.140	NGC 4289	449	Sbc	1.059 ± 0.081
PCCS1 857 G277.07+72.84	185.31732	11.50735	1.937 ± 0.153	NGC 4294	465	Sc	1.939 ± 0.144
PCCS1 857 G277.41+72.86	185.41840	11.48644	1.176 ± 0.160	NGC 4299	491	Scd	1.112 ± 0.093
PCCS1 857 G272.51+75.68	185.42477	14.59761	8.296 ± 0.168	NGC 4298/4302	483/497	Sc/Sc	12.573 ± 0.651
PCCS1 857 G284.35+66.28	185.47457	04.47981	17.872 ± 0.226	M 61	508	Sc	20.528 ± 1.455
PCCS1 857 G280.61+70.62	185.53208	09.03536	2.147 ± 0.136	NGC 4307	524	Sbc	1.757 ± 0.127
PCCS1 857 G282.47+68.84	185.55513	07.13962	0.828 ± 0.160	NGC 4309	534	Sa	0.603 ± 0.060
PCCS1 857 G284.61+66.39	185.60479	04.55969	0.822 ± 0.137	NGC 4301	552	Sc	0.454 ± 0.049
PCCS1 857 G271.42+76.60	185.63878	15.53121	1.516 ± 0.168	NGC 4312	559	Sab	1.532 ± 0.113
PCCS1 857 G277.71+73.24	185.65326	11.80437	1.706 ± 0.144	NGC 4313	570	Sab	1.586 ± 0.119
PCCS1 857 G280.71+70.96	185.67829	09.34033	2.502 ± 0.177	NGC 4316	576	Sbc	1.941 ± 0.142
PCCS1 857 G270.81+76.99	185.71130	15.93892	1.098 ± 0.200	· · ·	· · ·	· · ·	· · ·
PCCS1 857 G271.17+76.89	185.73530	15.81529	17.639 ± 0.257	M 100	596	Sc	25.968 ± 1.840
PCCS1 857 G284.50+67.11	185.77029	05.26741	0.933 ± 0.146	NGC 4324	613	Sa	0.722 ± 0.061
PCCS1 857 G278.76+72.90	185.80843	11.36855	1.634 ± 0.131	NGC 4330	630	Sd	1.547 ± 0.118
PCCS1 857 G282.91+69.24	185.83429	07.47657	1.941 ± 0.177	NGC 4334	638		1.736 ± 0.127
PCCS1 857 G283.52+68.77	185.90001	06.96069	2.263 ± 0.164	NGC 4343	656	Sb	1.517 ± 0.113
PCCS1 857 G282.53+70.30	186.03782	08.52197	0.821 ± 0.153	NGC 4356	713	Sc	0.539 ± 0.047
PCCS1 857 G283.94+69.33	186.21012	07.44889	0.963 ± 0.155	NGC 4370	758	S0	0.734 ± 0.057
PCCS1 857 G286.12+66.93	186.33071	04.92117	1.192 ± 0.134	NGC 4378	785	Sa	1.298 ± 0.105
PCCS1 857 G285.56+67.74	186.33387	05.75341	0.904 ± 0.155	NGC 4376	787	Scd	0.506 ± 0.044
PCCS1 857 G281.96+71.82	186.35291	10.02117	2.201 ± 0.156	NGC 4380	792	Sab	2.001 ± 0.149
PCCS1 857 G284.72+69.17	186.43134	07.21570	2.705 ± 0.162	UGC 7513	827	Sc	2.171 ± 0.157
PCCS1 857 G279.14+74.33	186.45118	12.66357	3.153 ± 0.176	NGC 4388	836	Sab	3.272 ± 0.234
PCCS1 857 G281.83+72.27	186.46056	10.45480	0.892 ± 0.154	NGC 4390	849	Sbc	0.833 ± 0.070
PCCS1 857 G284.56+69.49	186.46772	07.53835	0.860 ± 0.162	IC 3322	851	Sc	0.785 ± 0.061
PCCS1 857 G287.41+65.54	186.48927	03.44221	1.990 ± 0.184	UGC 7522	859	Sc	1.167 ± 0.087
PCCS1 857 G274.37+77.10	186.49855	15.66868	1.950 ± 0.170	NGC 4396	865	Sc	1.823 ± 0.135
PCCS1 857 G278.75+74.77	186.51927	13.10641	5.638 ± 0.161	NGC 4402	873	Sc	5.606 ± 0.396
PCCS1 857 G279.83+74.35	186.63556	12.60895	1.243 ± 0.171	NGC 4407	912	Sbc	1.058 ± 0.081
PCCS1 857 G287.47+66.09	186.64485	03.96705	1.378 ± 0.142	NGC 4412	921	Sbc	1.040 ± 0.079
PCCS1 857 G284.86+69.93	186.69124	07.92894	0.939 ± 0.123	NGC 4416	938	Sc	1.011 ± 0.081
PCCS1 857 G284.05+70.86	186.69953	08.90471	1.128 ± 0.147	UGC 7546	939	Sc	1.115 ± 0.108
PCCS1 857 G276.41+76.63	186.72600	15.04733	4.248 ± 0.195	NGC 4419	958	Sa	3.090 ± 0.220
PCCS1 857 G285.63+69.32	186.78597	07.27420	0.879 ± 0.172	UGC 7557	975	Scd	0.692 ± 0.069
PCCS1 857 G283.86+71.40	186.79590	09.43363	1.308 ± 0.147	NGC 4424	979	Sa	0.931 ± 0.073
PCCS1 857 G286.66+67.97	186.79940	05.87693	0.772 ± 0.142	NGC 4423	971	Sd	0.509 ± 0.043
PCCS1 857 G286.52+68.35	186.84390	06.25747	1.927 ± 0.162	NGC 4430	1002	Sc	1.654 ± 0.125
PCCS1 857 G282.36+73.01	186.85696	11.11080	0.904 ± 0.137	NGC 4429	1003	S0/a	0.672 ± 0.052

Notes. The first four columns list the PCCS name, the J2000 position of the *Planck* PCCS source, and the observed PCCS 857 GHz flux density with its associated error (the listed flux density is the standard DETFLUX estimate, see Sect. 3.1 for details). The following three columns give the name of the optical counterpart (if any), the VCC number, and the galaxy type (from the GOLDMine database). The last column lists the HeViCS SPIRE 350 μm flux density and its associated error for the sources with an identified counterpart. Details on how this flux density has been obtained can be found in Sect. 3.1.

Table 1. Continued.

PCCS source	α_{J2000} (deg)	δ_{J2000} (deg)	PCCS 857 GHz (Jy)	Counterpart	VCC	Type	SPIRE 350 μm (Jy)
PCCS1 857 G280.30+74.83	186.92881	13.01208	3.006 ± 0.153	NGC 4438	1043	Sb	3.373 ± 0.257
PCCS1 857 G285.11+71.32	187.16366	09.24766	1.104 ± 0.138	NGC 4451	1118	Sc	0.847 ± 0.068
PCCS1 857 G289.14+65.84	187.25201	03.57333	1.763 ± 0.135	NGC 4457	1145	Sb	1.600 ± 0.116
PCCS1 857 G286.11+70.88	187.35918	08.73663	1.198 ± 0.150	NGC 4469	1190	Sa	0.788 ± 0.061
PCCS1 857 G287.55+69.00	187.36934	06.79160	0.778 ± 0.143	IC 3414	1189	Sc	0.367 ± 0.036
PCCS1 857 G286.91+70.02	187.39922	07.83258	1.031 ± 0.142	NGC 4470	1205	Sc	0.977 ± 0.076
PCCS1 857 G289.65+66.56	187.60654	04.23901	1.607 ± 0.136	NGC 4480	1290	Sb	1.394 ± 0.104
PCCS1 857 G283.74+74.48	187.69562	12.38577	1.041 ± 0.169	M 87	1316	E	0.941 ± 0.074
PCCS1 857 G287.69+70.33	187.73649	08.07343	0.961 ± 0.145	NGC 4492	1330	Sa	0.597 ± 0.054
PCCS1 857 G290.53+66.33	187.90427	03.93704	4.098 ± 0.174	NGC 4496	1375	Sc	3.641 ± 0.260
PCCS1 857 G282.29+76.51	187.99116	14.43010	18.381 ± 0.246	M 88	1401	Sbc	22.165 ± 1.564
PCCS1 857 G283.78+75.59	188.04652	13.44229	0.775 ± 0.141	NGC 4506	1419	Sa	0.178 ± 0.026
PCCS1 857 G283.51+76.21	188.17680	14.05463	1.165 ± 0.142	IC 3476	1450	Sc	1.085 ± 0.092
PCCS1 857 G289.13+71.03	188.36439	08.64580	2.403 ± 0.152	NGC 4519	1508	Sc	2.268 ± 0.170
PCCS1 857 G288.89+71.57	188.40485	09.19277	1.873 ± 0.145	NGC 4522	1516	Sc	1.434 ± 0.107
PCCS1 857 G290.13+70.13	188.50485	07.69646	3.638 ± 0.163	NGC 4526	1535	S0	2.857 ± 0.207
PCCS1 857 G286.15+75.39	188.57616	13.08787	1.077 ± 0.167	NGC 4531	1552	Sa	0.590 ± 0.051
PCCS1 857 G290.06+70.64	188.58279	08.20291	8.869 ± 0.185	NGC 4535	1555	Sc	14.235 ± 1.024
PCCS1 857 G291.04+68.93	188.58782	06.46346	3.274 ± 0.166	NGC 4532	1554	Sm	2.893 ± 0.206
PCCS1 857 G290.87+69.64	188.65963	07.16808	0.886 ± 0.142	IC 3521	1575	Sm	0.631 ± 0.055
PCCS1 857 G285.72+76.81	188.86411	14.47983	4.691 ± 0.173	M 91	1615	Sb	6.128 ± 0.482
PCCS1 857 G289.78+73.72	189.13379	11.23932	15.958 ± 0.216	NGC 4567/4568	1673/1676	Sc/Sc	15.196 ± 1.281
PCCS1 857 G288.41+75.62	189.19517	13.17062	7.469 ± 0.162	M 90	1690	Sab	8.169 ± 0.581
PCCS1 857 G287.53+76.64	189.23359	14.21160	3.749 ± 0.197	NGC 4571	1696	Sab	3.597 ± 0.275
PCCS1 857 G290.38+74.34	189.42769	11.81137	6.354 ± 0.189	M 58	1727	Sab	8.286 ± 0.616

Table 2. Same as Table 1, but for the 545 GHz PCCS sources.

PCCS source	α_{J2000} (deg)	δ_{J2000} (deg)	PCCS 545 GHz (Jy)	Counterpart	VCC	Type	SPIRE 500 μm (Jy)
PCCS1 545 G260.37+75.43	182.66285	16.04584	0.922 ± 0.114	NGC 4152	25	Sc	0.735 ± 0.061
PCCS1 545 G276.77+67.93	183.25488	07.03960	0.533 ± 0.104	NGC 4180	73	Sb	0.562 ± 0.044
PCCS1 545 G268.38+73.71	183.44879	13.41927	0.498 ± 0.097	NGC 4189	89	Sc	0.911 ± 0.072
PCCS1 545 G265.43+74.97	183.46130	14.91524	2.640 ± 0.107	M 98	92	Sb	4.301 ± 0.318
PCCS1 545 G268.93+73.49	183.47034	13.15472	0.548 ± 0.111	NGC 4193	97	Sc	0.646 ± 0.060
PCCS1 545 G278.92+66.95	183.64901	05.81566	0.654 ± 0.111	NGC 4197	120	Scd	0.670 ± 0.054
PCCS1 545 G278.07+68.11	183.77733	07.01443	0.493 ± 0.094	⋯	⋯	⋯	⋯
PCCS1 545 G270.22+73.54	183.81908	13.01133	0.838 ± 0.103	NGC 4206	145	Sc	0.954 ± 0.076
PCCS1 545 G268.88+74.36	183.91488	13.90592	0.148 ± 0.106	NGC 4212	157	Sc	1.650 ± 0.123
PCCS1 545 G270.44+73.74	183.97938	13.16155	2.269 ± 0.099	NGC 4216	167	Sb	3.454 ± 0.252
PCCS1 545 G270.53+73.94	184.09985	13.31559	0.814 ± 0.103	NGC 4222	187	Scd	0.694 ± 0.057
PCCS1 545 G267.22+75.46	184.13517	15.07150	0.559 ± 0.105	⋯	⋯	⋯	⋯
PCCS1 545 G267.21+75.76	184.29853	15.32441	0.807 ± 0.105	NGC 4237	226	Sc	0.994 ± 0.077
PCCS1 545 G270.36+75.19	184.69368	14.43079	4.538 ± 0.116	M 99	307	Sc	7.927 ± 0.564
PCCS1 545 G282.53+66.97	184.99044	05.36161	0.942 ± 0.109	NGC 4273	382	Sc	1.368 ± 0.108
PCCS1 545 G277.04+72.84	185.30844	11.50868	0.707 ± 0.139	NGC 4294	465	Sc	0.805 ± 0.064
PCCS1 545 G272.43+75.68	185.41151	14.61110	2.796 ± 0.120	NGC 4298/4302	483/497	Sc/Sc	4.454 ± 0.325
PCCS1 545 G284.36+66.28	185.47873	04.48218	4.789 ± 0.116	M 61	508	Sc	7.050 ± 0.502
PCCS1 545 G280.54+70.63	185.50988	09.04869	0.569 ± 0.114	NGC 4307	524	Sbc	0.623 ± 0.050
PCCS1 545 G271.16+76.88	185.72922	15.81079	4.626 ± 0.114	M 100	596	Sc	8.825 ± 0.638
PCCS1 545 G278.76+72.88	185.80236	11.35158	0.523 ± 0.100	NGC 4330	630	Sd	0.635 ± 0.053
PCCS1 545 G281.96+71.79	186.34195	09.99236	0.708 ± 0.115	NGC 4380	792	Sab	0.709 ± 0.059
PCCS1 545 G284.73+69.17	186.43614	07.21787	1.125 ± 0.129	UGC 7513	827	Sc	0.908 ± 0.071
PCCS1 545 G279.13+74.34	186.45220	12.66788	0.964 ± 0.111	NGC 4388	836	Sab	1.218 ± 0.093
PCCS1 545 G274.40+77.10	186.50366	15.65977	0.640 ± 0.114	NGC 4396	865	Sc	0.771 ± 0.062
PCCS1 545 G287.46+65.53	186.50593	03.43199	0.664 ± 0.133	UGC 7522	859	Sc	0.526 ± 0.045
PCCS1 545 G278.76+74.77	186.52223	13.10600	1.747 ± 0.116	NGC 4402	873	Sc	1.951 ± 0.142
PCCS1 545 G284.05+70.82	186.68484	08.86340	0.655 ± 0.114	UGC 7546	939	Sc	0.538 ± 0.060
PCCS1 545 G276.42+76.65	186.73352	15.05677	0.834 ± 0.125	NGC 4419	958	Sa	1.074 ± 0.934
PCCS1 545 G286.60+68.36	186.87344	06.25631	0.664 ± 0.103	NGC 4430	1002	Sc	0.599 ± 0.052
PCCS1 545 G280.36+74.81	186.93803	12.98807	1.026 ± 0.134	NGC 4438	1043	Sb	1.208 ± 0.110
PCCS1 545 G289.65+66.58	187.61114	04.25924	0.503 ± 0.097	NGC 4480	1290	Sb	0.551 ± 0.045
PCCS1 545 G283.76+74.47	187.69775	12.37910	1.639 ± 0.096	M 87	1316	E	1.244 ± 0.094
PCCS1 545 G290.54+66.32	187.90694	03.92769	1.329 ± 0.119	NGC 4496	1375	Sc	1.423 ± 0.106
PCCS1 545 G282.29+76.51	187.99024	14.42921	5.887 ± 0.120	M 88	1401	Sbc	7.886 ± 0.558
PCCS1 545 G287.49+72.83	188.27660	10.51415	0.548 ± 0.112	⋯	⋯	⋯	⋯
PCCS1 545 G289.12+71.03	188.35920	08.65074	0.877 ± 0.109	NGC 4519	1508	Sc	0.907 ± 0.075
PCCS1 545 G288.90+71.54	188.40228	09.16123	0.537 ± 0.090	NGC 4522	1516	Sbc	0.539 ± 0.044
PCCS1 545 G290.14+70.13	188.50820	07.69494	0.780 ± 0.103	NGC 4526	1535	S0	0.929 ± 0.071
PCCS1 545 G289.64+71.15	188.55205	08.73088	0.612 ± 0.122	⋯	⋯	⋯	⋯
PCCS1 545 G291.04+68.92	188.58393	06.44702	0.827 ± 0.088	NGC 4532	1554	Sm	1.099 ± 0.081
PCCS1 545 G290.09+70.63	188.58932	08.18835	2.967 ± 0.110	NGC 4535	1555	Sb	5.387 ± 0.408
PCCS1 545 G285.69+76.83	188.86145	14.49705	1.525 ± 0.096	M 91	1615	Sb	2.065 ± 0.154
PCCS1 545 G286.36+76.69	188.97390	14.32142	0.568 ± 0.115	⋯	⋯	⋯	⋯
PCCS1 545 G289.82+73.73	189.14824	11.24395	4.231 ± 0.113	NGC 4567/4568	1673/1676	Sc/Sc	5.197 ± 0.447
PCCS1 545 G288.44+75.62	189.20407	13.16827	2.241 ± 0.106	M 90	1690	Sab	2.849 ± 0.210
PCCS1 545 G287.49+76.66	189.22770	14.22749	0.947 ± 0.130	NGC 4571	1696	Sc	1.182 ± 0.103
PCCS1 545 G290.37+74.35	189.42504	11.82011	1.887 ± 0.100	M 58	1727	Sab	2.877 ± 0.218